Frontiers of Materials Science

Electronic Supplementary Material

Flexible three-unit spatially encoded triboelectric sensor array for discrete bending–twisting decoding and wrist-motion recognition

Yun Yang (✉)[1], Shuohao Li[1], Chenyi Geng[2], Danyang He[1], Chengfei Jiang[1], and Tingting Cai[2]

1 Department of Resource and Mechanical Engineering, Lyuliang University, Lvliang 033001, China

2 Department of Chemical and Material Engineering, Lyuliang University, Lvliang 033001, China

E-mail: yangyun@llu.edu.cn

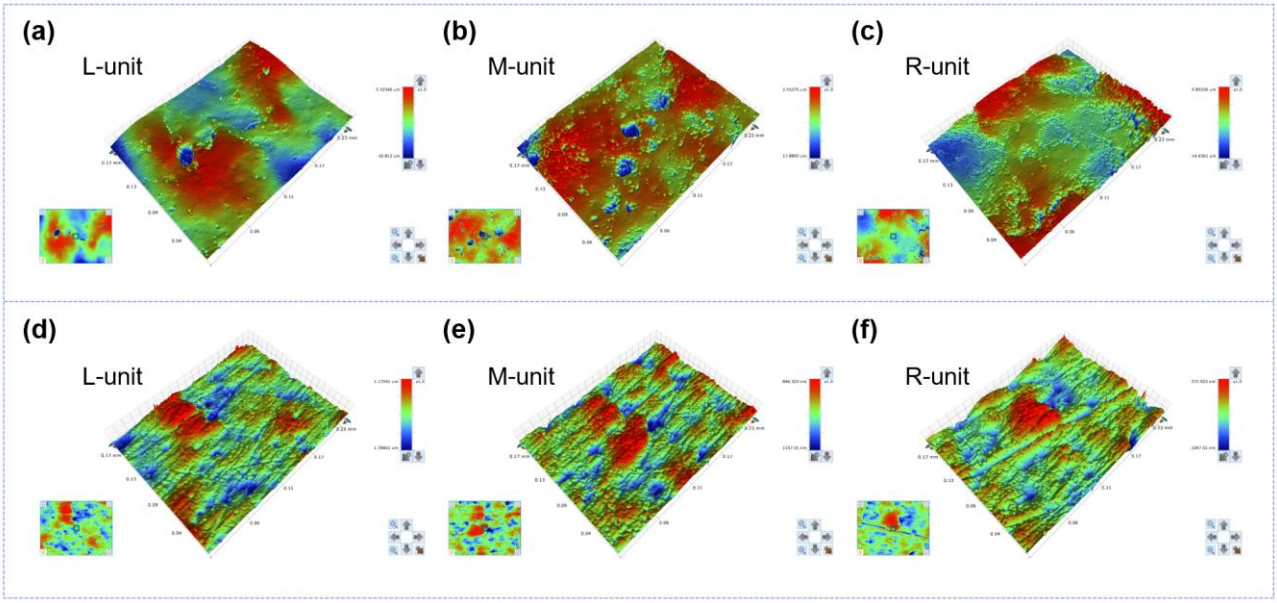


Fig. S1 Representative local surface topographies of the Cu electrodes and fused deposition modeling (FDM)-printed thermoplastic elastomer (TPE) at the three sensing regions: **(a)(b)(c)** Cu electrode surfaces at the regions corresponding to the L-, M-, and R-units, respectively; **(d)(e)(f)** FDM-printed TPE surfaces at the regions corresponding to the L-, M-, and R-units, respectively. The corresponding surface-roughness parameters are summarized in Table S2. The height scale shown in each panel corresponds to the individual local scan.

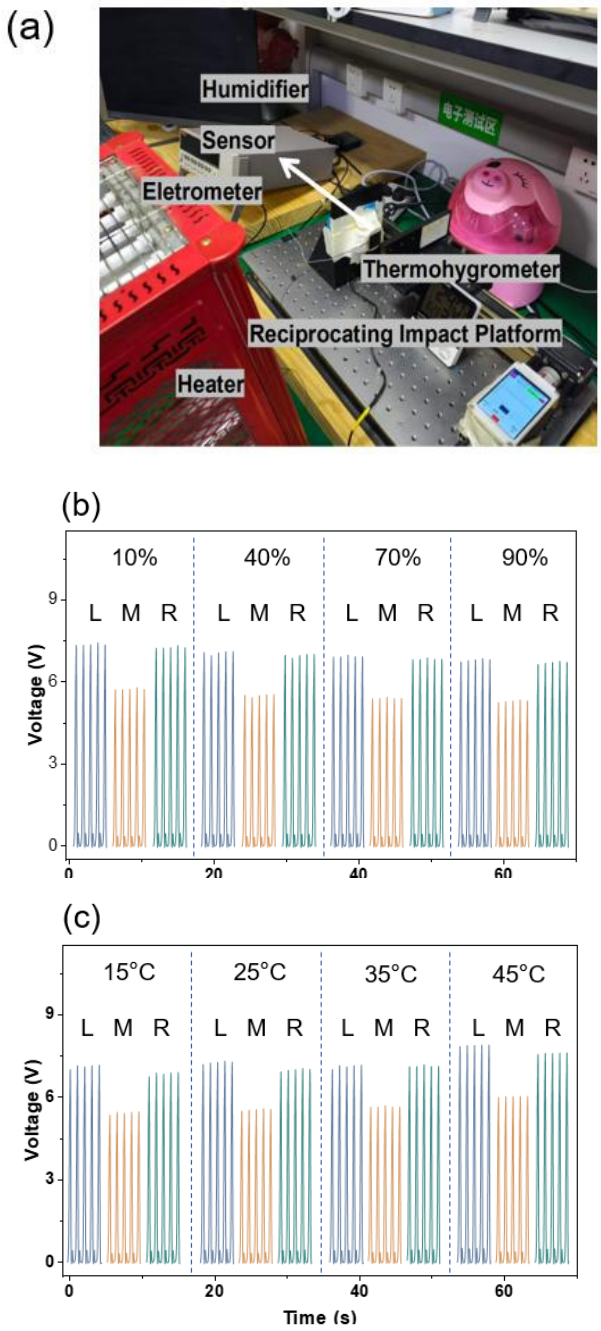


Fig. S2 Environmental response of the three-unit triboelectric sensor array under different relative humidity and temperature conditions: **(a)** Experimental setup for environmental-response testing; **(b)** Representative output waveforms of the L-, M-, and R-units at relative humidity (RH) of 10%, 40%, 70%, and 90% RH with the temperature maintained at 25 °C; **(c)** Representative output waveforms at temperatures of 15, 25, 35, and 45 °C with the relative humidity maintained at 40% RH. A periodic pressing load of 10 N at 1 Hz was applied under all conditions.

Note: As shown in Fig. S2, the L-, M-, and R-units maintained clear periodic outputs throughout the tested humidity and temperature ranges. Increasing relative humidity produced only modest changes in output amplitude, which may be partly associated with the polyurethane-film encapsulation, which reduces direct exposure of the triboelectric interfaces to ambient moisture, while increasing temperature resulted in a slight increase in output amplitude.

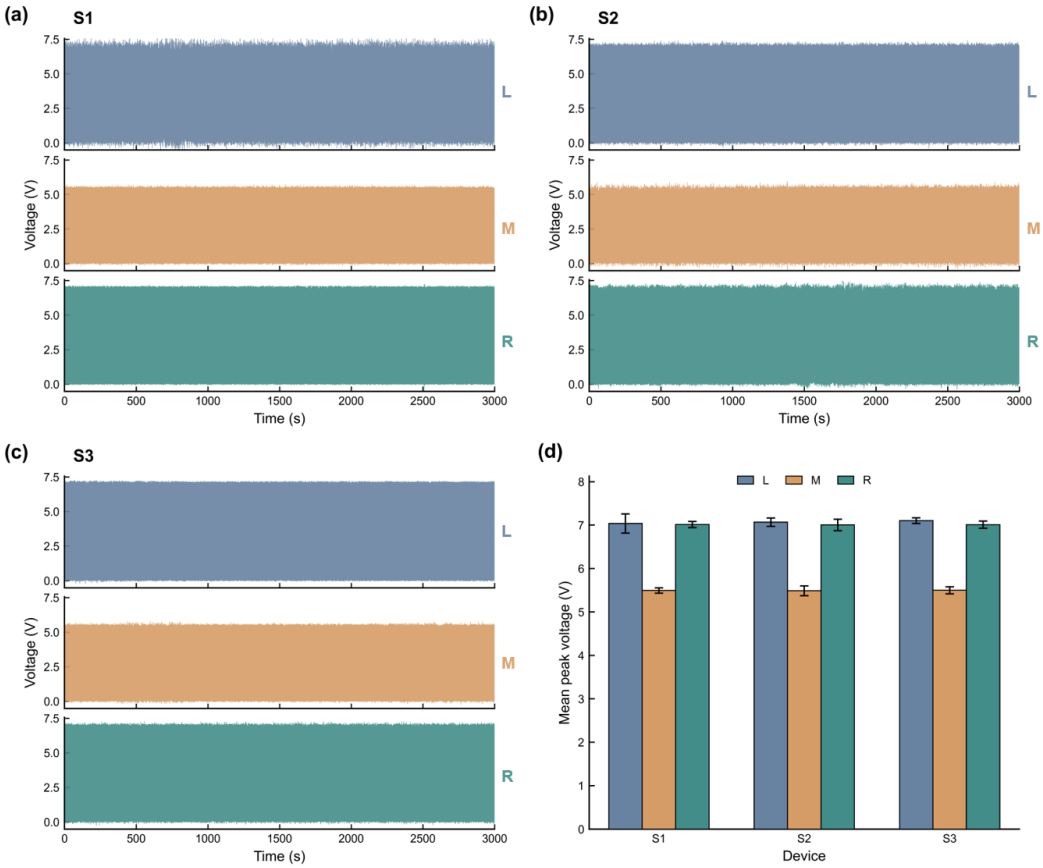


Fig. S3 Cyclic stability and device-to-device repeatability of the three-unit triboelectric sensor array: **(a)(b)(c)** Continuous output waveforms of the L-, M-, and R-units from three independently fabricated devices (S1, S2, and S3, respectively) during 3000 s of periodic pressing at 10 N and 1 Hz; **(d)** Mean peak voltages of the L-, M-, and R-units for the three devices (the error bars represent the standard deviations of the cycle peak voltages within each 3000 s recording).

Note: As shown in Fig. S3, all three independently fabricated devices maintained stable periodic outputs over approximately 3000 loading cycles. Across the nine device-unit recordings, the cycle-to-cycle coefficients of variation of the peak voltage ranged from 0.91% to 3.13%, while the maximum change between the mean peak voltages of the first and last 10% of cycles was 0.88%. The device-to-device coefficients of variation of the mean peak voltage were 0.47%, 0.12%, and 0.06% for the L-, M-, and R-units, respectively, indicating limited variation among the three independently fabricated devices under the tested conditions.

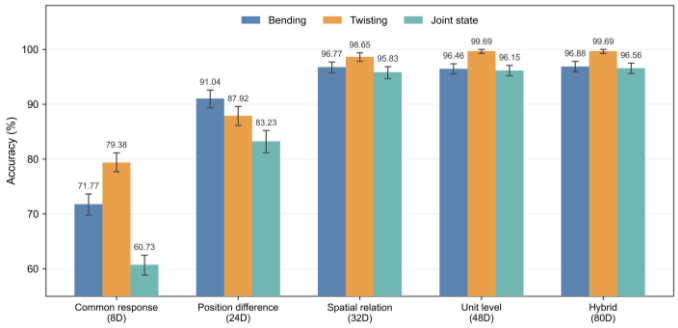


Fig. S4 Feature-representation ablation for discrete bending–twisting decoding.

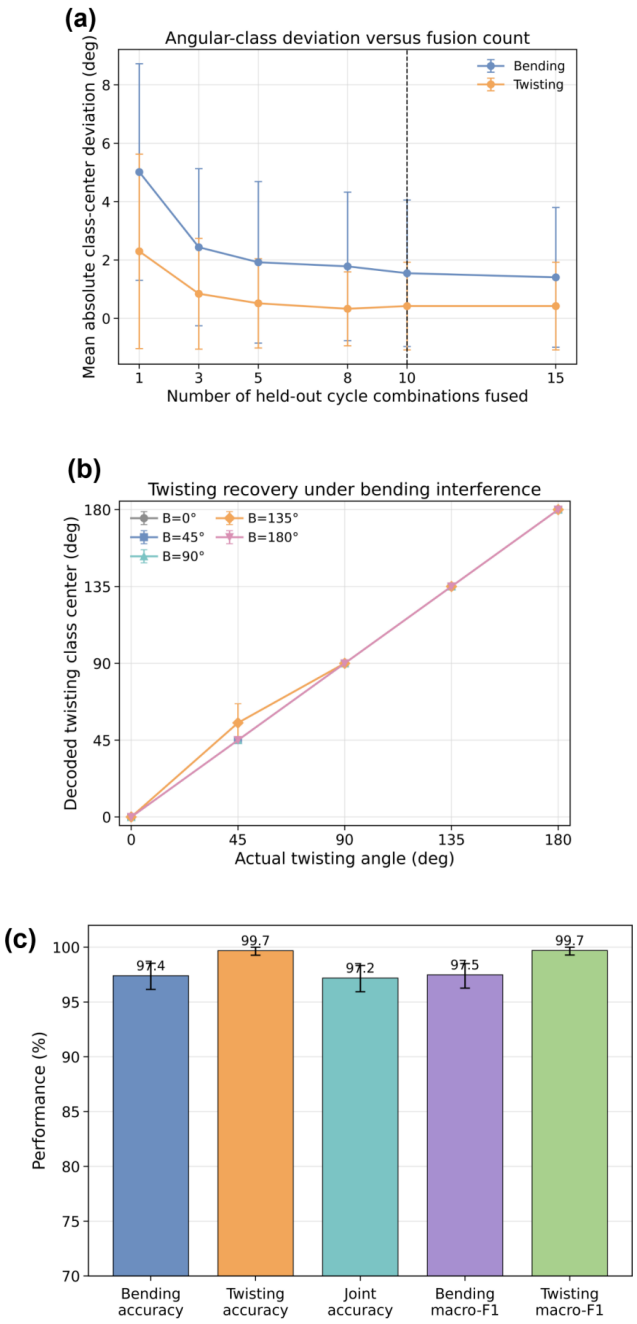


Fig. S5 Supplementary performance evaluation of discrete bending-twisting state decoding: **(a)** Variations in the mean absolute discrete-class-center deviations for bending and twisting with the number of fused held-out cycle combinations (the dashed line indicates the fusion of 10 combinations used in the main-text analysis, and the error bars represent the standard deviations across 40 repeated train-test splits); **(b)** Recovery of twisting states under different bending backgrounds (the dashed line indicates the ideal 1:1 correspondence, and the error bars represent the 95% confidence intervals); **(c)** Bending recognition accuracy, twisting recognition accuracy, joint-state recognition accuracy, and macro-averaged F1 scores for bending and twisting. A joint prediction was counted as correct only when both the bending and twisting classes were correctly predicted. The bar heights represent the means across 40 repeated splits, and the error bars represent the 95% bootstrap confidence intervals calculated using the repeated splits as the resampling units. The class centers and class-center deviations in Panels (a) and (b) were calculated from the final discrete class predictions after probability fusion and do not represent continuous angle-regression results.

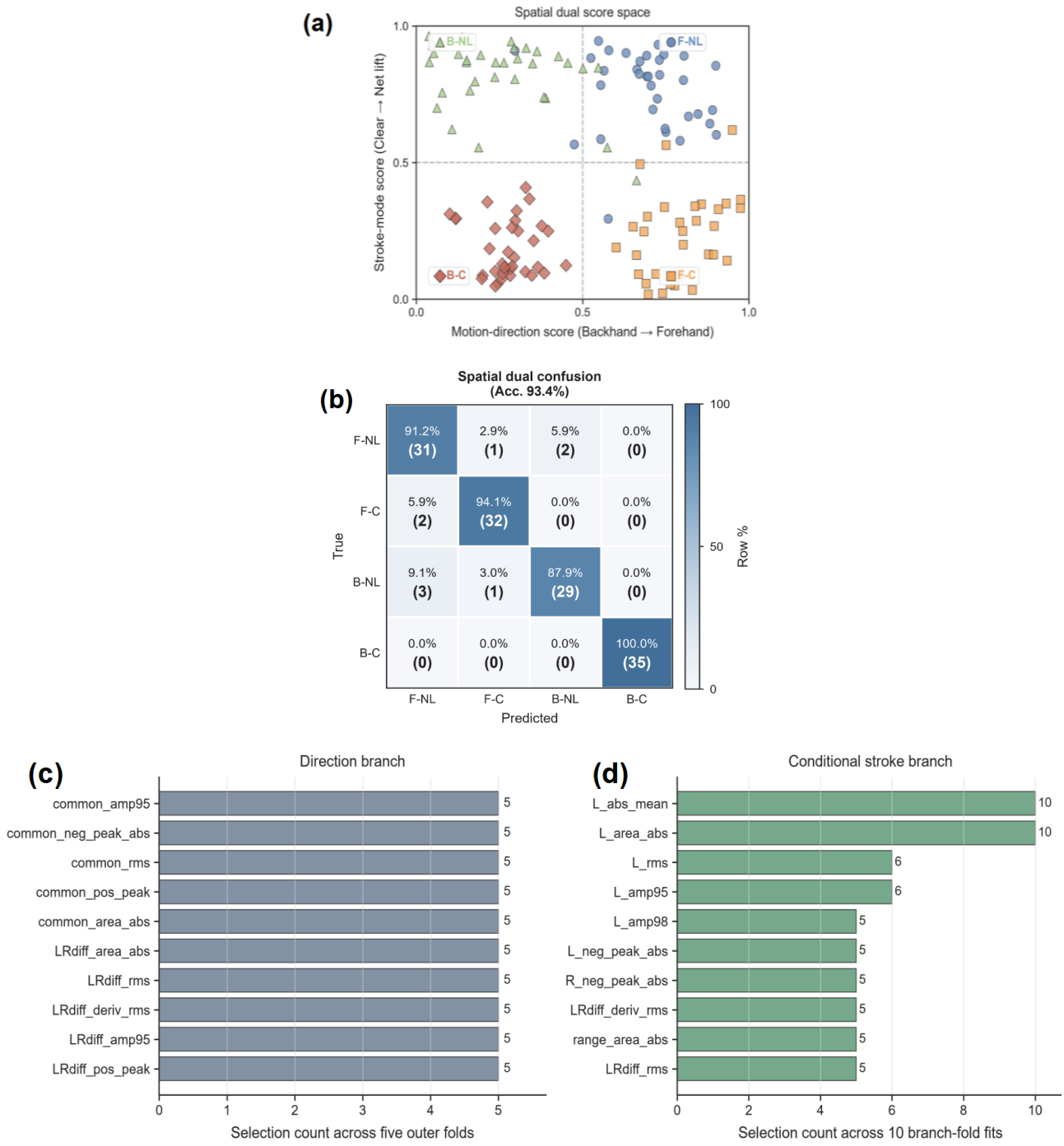


Fig. S6 Supplementary model results and feature-selection frequencies for badminton wrist-motion recognition: **(a)** Sample distribution of the Spatial dual model in the two-dimensional motion direction-stroke mode score space (the horizontal and vertical axes represent the support vector machine decision scores for motion direction and stroke mode, respectively, after transformation using a sigmoid function; the dashed lines indicate the visualization boundaries at 0.5; these scores were used only for visualization and were not interpreted as calibrated class probabilities); **(b)** Row-normalized four-motion confusion matrix of the Spatial dual model, with the sample counts shown in parentheses; **(c)** Number of times each major feature was selected across the five outer validation folds in the motion-direction branch of the Conditional dual model; **(d)** Cumulative feature-selection counts across 10 branch-model fits in the forehand- and backhand-conditioned stroke-mode branches. F-NL, F-C, B-NL, and B-C denote forehand lift, forehand clear, backhand lift, and backhand clear, respectively.

Note: The feature labels in the figure are defined as follows: common_amp95, common response of the 5%–95% robust amplitude across the three positions; common_neg_peak_abs, common response of the robust negative-peak absolute value across the three positions; common_rms, common response of the root mean square across the three positions; common_pos_peak, common response of the robust positive peak across the three positions; common_area_abs, common response of the waveform absolute area across the three positions; LRdiff_area_abs, normalized left–right difference in waveform absolute area; LRdiff_rms, normalized left–right difference in root mean square; LRdiff_deriv_rms, normalized left–right difference in the root mean square of the first difference; LRdiff_amp95, normalized left–right difference in the 5%–95% robust amplitude; LRdiff_pos_peak, normalized left–right difference in the robust positive peak; L_abs_mean, mean absolute value of the L-unit waveform; L_area_abs, absolute area of the L-unit waveform; L_rms, root mean square of the L-unit waveform; L_amp95, 5%–95% robust amplitude of the L-unit; L_amp98, 2%–98% robust amplitude of the L-unit; L_neg_peak_abs, robust negative-peak absolute value of the L-unit; R_neg_peak_abs, robust negative-peak absolute value of the R-unit; and range_area_abs, normalized three-position range of the waveform absolute area. The label common denotes the arithmetic mean of the feature values across the three positions.

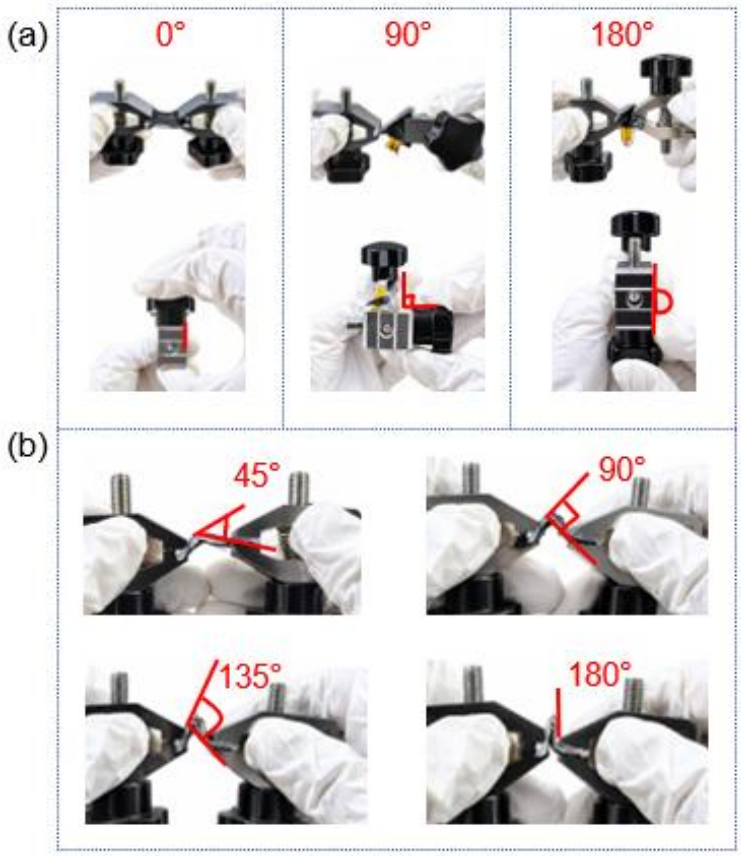


Fig. S7 Geometrical definitions and representative experimental configurations of twisting and bending angles: **(a)** Representative configurations at twisting angles of 0°, 90°, and 180°, shown from two viewing directions (the twisting angle is defined as the relative rotation of the movable end with respect to the fixed end about the longitudinal axis of the device); **(b)** Representative configurations at bending angles of 45°, 90°, 135°, and 180° (the bending angle is defined as the rotation of the movable end relative to its initial straight orientation within the bending plane).

Table S1 Comparison of representative multi-unit flexible sensing architectures, information representations, and decoding strategies

Ref.	Sensor architecture	Unit configuration/ relationship	Target information	Multi-unit/multi-channel representation	Decoding/ output
[S1]	8 × 8 fabric-based triboelectric touch array	Row-column intersection pixels with grounded crosstalk shielding	Touch position, contact profile, and trajectory	Row-column activation patterns	Threshold-based position/profile mapping and trajectory tracking
[S2]	Three-unit FDM-FPC TENG smart insole	Three homogeneous TENG units at the medial forefoot, heel, and lateral forefoot	Five race-walking states	CH1-CH3 + magnitude + first derivatives (7 channels)	Multi-scale CNN-BiGRU five-class classification
[S3]	Symmetric dual-output TENG multidimensional force sensor	Two semicircular electrodes; shear-induced contact offset yields asymmetric outputs	Normal and shear force	V1 + V2 (normal) and V2/V1 (shear)	Calibration-based algebraic force decoupling (validated range)
[S4]	Multi-channel textile TENG bending sensor	Co-located homogeneous units arranged at different orientations	Bending angle, direction, and speed	Voltage amplitude (angle), relative channel response (direction), and voltage-change rate (speed)	Calibration-based angle/speed estimation; relative-response direction identification
[S5]	Four-channel wearable TENG neck-motion sensor	Four homogeneous TENGs spatially distributed around a collar	11 neck-motion classes	Four-channel voltage time series with motion-dependent amplitude and polarity patterns	CNN-based 11-class motion classification
[S6]	Three-unit multimodal flexible sensor	Three co-located heterogeneous units: optoelectronic, ionic-liquid resistive, and conductive-fabric resistive	Pressing, bending, twisting, and combined deformations	Photodiode voltage + ionic-liquid frequency + conductive-fabric resistance	Transformer-based decoupling and deformation-magnitude prediction
This work	Three-unit flexible triboelectric sensor	Same material system and nominally identical basic configuration	Coupled bending-twisting states	Unit-level waveform descriptors + explicit inter-unit spatial-relation features [1)]	Feature-level spatial encoding for separate bending and twisting decoding

1) Spatial-relation features: common response, left-right difference, center deviation, and inter-unit range.

Notes: BiGRU, bidirectional gated recurrent unit; CNN, convolutional neural network; FDM, fused deposition modeling; FPC, flexible printed circuit; TENG, triboelectric nanogenerator.

References

[S1] Zhu X X, Meng X S, Kuang S Y, et al. Triboelectrification-enabled touch sensing for self-powered position mapping and dynamic tracking by a flexible and area-scalable sensor array. Nano Energy, 2017, 41: 387–393

[S2] Yang Y, Zhang Z, Cai T, et al. Standardized batch-manufacturable triboelectric sensor arrays for deep learning-enabled race-walking state recognition. Chemical Engineering Journal, 2026, 542: 178259

[S3] Wang Z, Bu T, Li Y, et al. Multidimensional force sensors based on triboelectric nanogenerators for electronic skin. ACS Applied Materials & Interfaces, 2021, 13: 56320–56328

[S4] Cao Y, Shao H, Wang H, et al. An easy-to-install textile bending sensor with high sensitivity, linearity, and multidirection direction capability. Advanced Materials Technologies, 2022, 7: 2100830

[S5] An S, Pu X, Zhou S, et al. Deep learning enabled neck motion detection using a triboelectric nanogenerator. ACS Nano, 2022, 16: 9359–9367

[S6] Yang C, Liu H, Ma J, Xu M. Multimodal flexible sensor for the detection of pressing-bending-twisting mechanical deformations. ACS Applied Materials & Interfaces, 2025, 17: 2413–2424

Table S2 Representative local surface roughness of the Cu electrodes and FDM-printed TPE at the regions corresponding to the L-, M-, and R-units

Material	Region	Roughness parameter	
		R_a/μm	R_q/μm
FDM-printed TPE	L region	1.144	1.466
	M region	0.867	1.450
	R region	1.407	1.792
Cu electrode	L region	132.3	172.2
	M region	109.3	142.8
	R region	145.2	187.8

Notes: R_a denotes the arithmetic-average roughness, and R_q denotes the root-mean-square roughness. One local surface scan was obtained for each material at each sensing region; therefore, the values are reported as representative local measurements rather than for statistical comparison among the three regions.

Table S3 Feature-representation ablation for discrete bending–twisting decoding

Feature representation	Dimension	Bending accuracy/% (95% CI)	Twisting accuracy/% (95% CI)	Joint state accuracy/% (95% CI)
Common response (8D)	8	71.77 (69.79–73.65)	79.38 (77.71–81.15)	60.73 (58.85–62.50)
Position difference (24D)	24	91.04 (89.38–92.60)	87.92 (86.15–89.58)	83.23 (81.15–85.21)
Spatial relation (32D)	32	96.77 (95.73-–97.71)	98.65 (97.81–99.38)	95.83 (94.69–96.88)
Unit level (48D)	48	96.46 (95.52–97.40)	99.69 (99.27–100.00)	96.15 (95.21–97.08)
Hybrid (80D)	80	96.88 (95.94–97.81)	99.69 (99.27–100.00)	96.56 (95.62–97.50)

Notes: All feature representations were evaluated under the same 40-repeat held-out-cycle validation framework. The same real-cycle splits, training and test combinations, classifier configuration, and 10-combination probability fusion were used within each comparison. The common-response and position-difference subsets together constitute the complete 32-dimensional spatial-relation representation. CI, confidence interval.

Table S4 Comparison between held-out-cycle and strict leave-one-coupled-combination-out validation for the same 16 coupled bending-twisting states

Validation	Bending accuracy/% (95% CI)	Twisting accuracy/% (95% CI)	Joint-state accuracy/% (95% CI)
Held-out-cycle	95.62 (94.06–97.03)	99.38 (98.75–99.84)	95.16 (93.59–96.56)
Strict LOCO	5.78 (4.22–7.19)	37.03 (35.78–38.28)	0.00

Notes: The held-out-cycle reference used the standard 70%/30% real-cycle split within each sensing unit and mechanical state, with all 24 measured states represented in training; performance was reported only for the same 16 coupled test states evaluated by LOCO. In strict LOCO validation, one complete coupled bending-twisting condition and all of its cycles were excluded from training in each fold, leaving 23 measured states for model training. Both validation procedures used the same 80-dimensional feature representation, classifier configuration, and probability fusion over 10 test combinations. Values are means over 40 complete repetitions, and 95% confidence intervals were obtained by 5000 bootstrap resamples with the complete repetition treated as the resampling unit.

Table S5 Definitions of the unit-level cycle features

Feature name	Mathematical definition or calculation method
5%–95% robust amplitude	$A_{95} = P_{95} - P_5$
2%–98% robust amplitude	$A_{98} = P_{98} - P_2$
Root mean square	Square root of the mean of the squared waveform values
Mean absolute value	Arithmetic mean of the absolute waveform values
Robust positive peak	$P_+ = \max(P_{95}, 0)$
Robust negative-peak absolute value	$P_- = \max(-P_5, 0)$
Peak-polarity asymmetry	$\frac{P_+ - P_-}{P_+ + P_- + \varepsilon}$
Integrated-polarity asymmetry	$\frac{S_+ - S_-}{S_+ + S_- + \varepsilon}$
Skewness	Third standardized moment of the waveform-amplitude distribution
Excess kurtosis	Fisher kurtosis of the waveform-amplitude distribution
First-difference root mean square	Root mean square of the differences between adjacent sampling points
Crest factor	Ratio of the maximum absolute amplitude to the root mean square
Zero-crossing rate	Proportion of adjacent sampling points with a change in sign
Second-harmonic ratio	$\frac{\lvert H_2 \rvert}{\lvert H_1 \rvert + \varepsilon}$
Third-harmonic ratio	$\frac{\lvert H_3 \rvert}{\lvert H_1 \rvert + \varepsilon}$
Original cycle length	Number of sampling points contained in the cycle before resampling

Notes: P_p denotes the pth percentile of the waveform amplitude; S_+ and S_- denote the absolute areas of the positive and negative half-waves, respectively; H_1, H_2, and H_3 denote the amplitudes of the first, second, and third non-direct-current frequency components obtained by applying a fast Fourier transform to the 128-point resampled waveform. Throughout Supplementary Notes S1.2 and S1.3, $\varepsilon = 1\times10^{-12}$ was used as a numerical-stability constant to prevent division by zero. The low-order frequency-component ratios were used only to describe the waveform shape of the resampled cycle and were not used to estimate the actual mechanical-motion frequency.

Note S1 Signal processing, feature representation, and discrete bending-twisting decoding

S1.1 Raw-signal preprocessing and cycle quality control

Each raw voltage recording was first subjected to linear detrending. The dominant motion period was then estimated from the power spectrum within a candidate range of 600–1300 sampling points. A second-order Savitzky–Golay filter was used to estimate the slowly varying baseline, with the filter-window length set to approximately three dominant motion periods. The smoothed baseline was subtracted from the detrended signal to obtain the baseline-corrected signal used for cycle segmentation.

Peak detection was performed on both the positive- and negative-polarity responses during cycle segmentation. The minimum peak distance was set to 0.55 times the estimated dominant motion period, and the peak-prominence threshold was set to the larger of 0.35 times the signal standard deviation and 0.04 times the signal peak-to-peak value. The midpoints between adjacent characteristic peaks were defined as the cycle boundaries, and only candidate cycles with lengths ranging from 0.55 to 1.55 times the estimated dominant motion period were retained. When fewer than four candidate cycles were obtained through peak detection, supplementary segmentation was performed using equally spaced windows based on the estimated dominant motion period.

Each candidate cycle was resampled to 128 data points. The robust cycle amplitude was defined as the difference between the 95th and 5th percentiles, and the pointwise median waveform of all candidate cycles within the same raw recording was used as the shape template. A cycle was identified as an outlier and excluded when its robust amplitude deviated from the median cycle amplitude of the recording by more than 3.5 robust standard deviations, or when its Pearson correlation coefficient with the median waveform template was not greater than 0.15. The robust standard deviation was calculated as the median absolute deviation multiplied by 1.4826.

When fewer than five cycles remained after threshold-based screening, the cycles were jointly ranked according to their standardized amplitude deviations and template-correlation coefficients, and at least five higher-quality cycles were retained. The bending angle, twisting angle, and mechanical-state labels were not used during cycle quality control.

S1.2 Unit-level cycle features

Let a baseline-corrected and median-centered cycle at its original segmented length be expressed as

$$\mathbf{x}=\left(x_1,x_2,\ldots,x_{n_0}\right) \tag{S1}$$

where n_0 denotes the number of sampling points contained in the segmented cycle. Unless otherwise specified, the unit-level features were calculated from $\mathbf{x}$ at this original segmented length. For calculation of the low-order harmonic ratios only, $\mathbf{x}$ was resampled to 128 points, which was denoted as

$$\tilde{\mathbf{x}} = (\tilde{x}_1, \tilde{x}_2, \ldots, \tilde{x}_{128}) \tag{S2}$$

For each sensing unit, the 16 features listed in Table S5 were extracted from each retained cycle.

The features from the L-unit, M-unit, and R-unit were sequentially concatenated to form a 48-dimensional unit-level feature representation.

S1.3 Three-unit spatial features

To describe the common responses and relative differences among the three sensing positions, spatial-relation features were further constructed from the following eight basic features: 5%–95% robust amplitude, root mean square, robust positive peak, robust negative-peak absolute value, peak-polarity asymmetry, integrated-polarity asymmetry, first-difference root mean square, and original cycle length. All spatial-relation descriptors were calculated from scalar cycle-level features independently extracted from the three sensing positions. They therefore characterize feature-level response relationships among the positions and do not require point-by-point temporal synchronization of the L-, M-, and R-unit waveforms.

For any basic feature, let its values for the L-unit, M-unit, and R-unit be denoted as f_{L}, f_{M}, and f_{R}, respectively.

The common response was defined as

$$f_{\mathrm{com}}=\frac{f_L+f_M+f_R}{3} \tag{S3}$$

which characterizes the mean response level of the three sensing units.

The normalized left-right difference was defined as

$$f_{\mathrm{LR}}=\frac{f_R-f_L}{|f_L|+|f_M|+|f_R|+\varepsilon} \tag{S4}$$

which describes the response asymmetry between the left and right sensing positions of the device.

The normalized center deviation was defined as

$$f_{\mathrm{mid}}=\frac{f_M-(f_L+f_R)/2}{|f_L|+|f_M|+|f_R|+\varepsilon} \tag{S5}$$

which describes the deviation of the middle sensing unit from the mean response of the two lateral units.

The normalized inter-unit range was defined as

$$f_{\mathrm{range}}=\frac{\max(f_L,f_M,f_R)-\min(f_L,f_M,f_R)}{|f_L|+|f_M|+|f_R|+\varepsilon} \tag{S6}$$

which describes the overall dispersion of responses among the three sensing positions.

The four spatial descriptors were calculated for each of the eight basic features, yielding 32 spatial-relation features. The 48-dimensional unit-level features and 32-dimensional spatial-relation features were combined to form an 80-dimensional feature representation used as the input to the bending and twisting classifiers.

S1.4 Train-test splitting, data augmentation, and classifiers

In each repeated analysis, the retained real cycles from each sensing unit under the same mechanical state were first divided into non-overlapping training and test pools at a ratio of 70% to 30%. The cycle splitting was performed separately for the L-unit, M-unit, and R-unit before constructing the three-unit training and test combinations, thereby preventing the same real cycle from entering both the training and test procedures.

Data augmentation was applied only to cycles in the training pool and included amplitude scaling of no more than ±1.5%, temporal stretching of no more than ±1.5%, random noise with a standard deviation equal to 0.8% of the standard deviation of the original cycle signal, and linear baseline drift with an amplitude no greater than 0.4% of the standard deviation of the original cycle signal. No data augmentation was applied to cycles in the test pool.

For each mechanical state, 25 three-unit training combinations and 15 three-unit test combinations were randomly constructed in each repeated split. Each combination consisted of one L-unit cycle, one M-unit cycle, and one R-unit cycle selected under the same nominal mechanical state. Because the three sensing units were acquired sequentially in separate recording runs, each L-, M-, and R-unit cycle originated from a separate recording under the same nominal mechanical condition. The three positions were therefore matched at the mechanical-condition level rather than by acquisition time, and no one-to-one temporal pairing among individual cycles was imposed. These combinations were used only to construct feature-level multi-position representations and do not indicate that the three cycles originated from the same synchronous loading event. Instantaneous phase relationships, peak-timing differences, and propagation delays among the units were not used. The cycle combinations were not treated as new independent mechanical experiments.

The bending and twisting states were predicted using two separate Extremely Randomized Trees classifiers. Each classifier consisted of 300 randomized decision trees. At each node split, a number of candidate features equal to the square root of the total number of input features was randomly selected. The minimum number of training samples required at a leaf node was set to 1, and the class weights were automatically adjusted according to the number of training samples in each class.

Both classifiers output five discrete angle classes of 0°, 45°, 90°, 135°, and 180°, corresponding to the bending and twisting states, respectively.

To additionally evaluate condition-wise generalization, a strict leave-one-coupled-combination-out (LOCO) validation was performed for the 16 coupled states with bending and twisting angles of 45°, 90°, 135°, and 180°. In each fold, all retained real cycles belonging to one coupled mechanical condition were completely excluded from model training, while the remaining 23 measured states were retained for training. The same 80-dimensional feature representation, training-only augmentation procedure, two separate 300-tree Extremely Randomized Trees classifiers, and probability fusion over 10 non-augmented test combinations were used. No cycle from the held-out mechanical condition was used for model fitting. The complete 16-fold procedure was repeated 40 times using different random seeds. For a matched reference, the standard held-out-cycle protocol was also evaluated with performance restricted to the same 16 coupled test states. In this reference protocol, all 24 measured states remained represented in the training data through the standard within-condition train-test split, whereas in strict LOCO validation the complete test condition was absent from training. The 95% confidence intervals were calculated using 5000 bootstrap resamples, with the 40 complete repetitions treated as the resampling units. The quantitative comparison between the two validation strategies is summarized in Table S4.

S1.5 Multi-cycle probability fusion and performance evaluation

For each three-unit test combination, the bending and twisting classifiers separately output the predicted probabilities for the five discrete angle classes. To reduce the influence of fluctuations in individual cycle combinations, recognition performance was evaluated by fusing 1, 3, 5, 8, 10, and 15 test combinations. During fusion, the probabilities of the same class output by multiple test combinations were averaged, and the class with the highest mean probability was selected as the final discrete prediction. The results reported in the main text were obtained using probability fusion over 10 test combinations.

To visualize the decoded discrete states in the two-dimensional bending–twisting space, a probability-weighted discrete-class score was calculated from the mean class probabilities as

$$s=\sum_{k=1}^{K}\bar{p}_k c_k \tag{S7}$$

where K = 5 is the number of discrete angle classes, $\bar{p}_k$ denotes the mean predicted probability of the k**th** discrete class after multi-cycle fusion, and c_k denotes the corresponding class center (0°, 45°, 90°, 135°, or 180°). This score was used only for visualization of the decoded state distribution in Fig. 4(d) and was not interpreted as a continuous angle estimate or angle-regression output.

The final discrete prediction was determined as the class with the highest mean probability,

$$\hat{c}=c_{\arg\max_k \bar{p}_k} \tag{S8}$$

Based on this final discrete prediction, the mean absolute discrete-class-center deviation was calculated as

$$D_{\text{class}}=\frac{1}{N}\sum_{i=1}^{N}\left|\hat{c}_i-c_i\right| \tag{S9}$$

where N is the number of state-level fused predictions included in the evaluation, c_i is the nominal discrete class center, and $\hat{c}_i$ is the final predicted discrete class center after probability fusion. This metric was used for Fig. 4(g) and Fig. S5(a), while the class-center recovery curves in Fig. 4(f) and Fig. S5(b) were calculated from the final discrete class predictions across the repeated analyses. Because the nominal class centers were separated by 45°, the discrete-class-center deviation characterizes the average distance between the predicted and nominal discrete classes. Neither this deviation metric nor the class-center recovery summaries should be interpreted as continuous angular resolution or continuous-angle measurement error.

The train-test splitting and model-training procedures were repeated 40 times using different random seeds. In each repetition, one multi-cycle fused prediction was generated for each of the 24 mechanical states, yielding a total of 960 state-level fused predictions. These 960 results were obtained from the combination of 40 repeated splits and 24 mechanical states and do not represent 960 mutually independent mechanical experiments.

Model performance was evaluated using bending recognition accuracy, twisting recognition accuracy, joint-state recognition accuracy, balanced accuracy, macro-averaged F1 score, and mean absolute discrete-class-center deviation. A joint prediction was counted as correct only when both the bending and twisting outputs were correctly predicted. The 95% confidence intervals were calculated using 5000 bootstrap resamples, with the 40 repeated analyses treated as the resampling units.

Principal component analysis was used only to visualize the feature-space distribution before decoding and was not involved in feature selection, classifier training, parameter setting, or performance calculation.

Note S2 Data processing, feature construction, and model evaluation for badminton motions

S2.1 Three-position sample organization and waveform preprocessing

The badminton wrist motions comprised four classes: forehand lift (F-NL), forehand clear (F-C), backhand lift (B-NL), and backhand clear (B-C). Signals from the L-unit, M-unit, and R-unit were acquired sequentially in separate recording runs and matched according to the original recording order within each motion class. For the same motion class, the ith L-unit, ith M-unit, and ith R-unit recordings jointly constituted the ith three-position motion sample. A total of 136 three-position

samples were obtained, including 34 F-NL, 34 F-C, 33 B-NL, and 35 B-C samples.

This sequence matching was used only for sample organization and for constructing feature-level multi-position representations within the same motion class and does not indicate that the three sensing units recorded synchronous signals from the same stroke. The sequence index therefore did not represent temporal alignment among the L-, M-, and R-unit recordings. Accordingly, instantaneous features based on phase differences, peak-timing differences, or signal-propagation delays among the units were not constructed in the subsequent analysis.

During waveform preprocessing, nonfinite values were first removed from each recording, and recordings containing fewer than 20 valid sampling points were excluded from subsequent analysis. The first and last 5% of the sampling points in each raw waveform were combined, and their overall median was subtracted as the edge baseline. Linear detrending was then applied to reduce slowly varying drift. Motion waveforms with different durations were resampled to 512 normalized time points using Fourier resampling. The resulting 512-point median-centered waveform was used as the input for badminton-motion feature extraction. The original recording length before resampling was retained separately for the recording-length feature.

No amplitude normalization was applied to individual waveforms before feature extraction, thereby preserving differences in response intensity among motion classes and sensing positions. The feature-standardization parameters required for model training were calculated only from the corresponding training data, and the same transformation was then applied to the test data.

The representative waveforms in Fig. 6(c) were used only for visualization. For each motion class, the corresponding class center was first calculated in the 32-dimensional spatial-relation feature space, and the three-position sample closest to that class center was selected as the representative sample. For plotting, each representative waveform from the L-unit, M-unit, and R-unit was individually offset by subtracting its own first resampled data point, so that the waveform was displayed relative to a zero starting level.

S2.2 Unit-level features and spatial-relation features

Sixteen unit-level features were extracted from each waveform to describe the robust amplitude, overall response intensity, positive- and negative-polarity responses, amplitude distribution, dynamic variation, low-order waveform shape, and original recording length before resampling. The feature definitions followed those listed in Table S5, while their calculation was adapted to the badminton-motion preprocessing described in Note S2.1. Specifically, waveform-derived features were calculated from the 512-point median-centered waveform, whereas the original recording length before resampling was retained separately as the length feature. The second- and third-harmonic ratios were calculated from the 512-point resampled waveform. The low-order frequency-component ratios were used only to characterize the shape of the time-resampled waveform and were not interpreted as the actual motion frequency.

The 16 features from the L-unit, M-unit, and R-unit were combined in a fixed order to form 48-dimensional multi-position unit-level features, thereby retaining the amplitude and waveform information from each of the three sensing positions.

Spatial-relation features were further constructed from the following eight basic descriptors: 5%–95% robust amplitude, root mean square, robust positive peak, robust negative-peak absolute value, peak-polarity asymmetry, integrated-polarity asymmetry, waveform absolute area, and first-difference root mean square.

The waveform absolute area was defined as the sum of the absolute values of the 512-point

resampled waveform. For each basic descriptor, the four spatial operations defined in Note S1.3, namely the common response, normalized left–right difference, normalized center deviation, and normalized inter-unit range, were calculated to generate 32 spatial-relation features. The same mathematical definitions and numerical-stability constant ε specified in Note S1.3 were used for these spatial operations. These spatial operations were applied only to the feature values from the three positions in sequence-matched samples within the same motion class and did not involve inter-position temporal alignment, phase relationships, peak-timing differences, or propagation-delay information.

The 48-dimensional multi-position unit-level features and 32-dimensional spatial-relation features were combined to form an 80-dimensional hybrid feature representation.

S2.3 Comparison models and conditional dual-task model

To compare single sensing positions, multi-position feature representations, and different task organizations, the following models were established:

"L only", "M only", and "R only": the 16-dimensional features from an individual sensing unit were used for four-class motion recognition;

"Direct 3-ch": the 48-dimensional multi-unit features formed by combining the three units were used for direct four-class classification;

"Spatial 4C": the 32-dimensional spatial-relation features were used for direct four-class classification;

"Hybrid 4C": the 80-dimensional hybrid features were used for direct four-class classification;

"Spatial dual": the 32-dimensional spatial-relation features were used to separately recognize the forehand/backhand motion direction and the lift/clear stroke mode, after which the outputs of the two tasks were combined;

"Hybrid dual": the 80-dimensional hybrid features were used to separately recognize the motion direction and stroke mode, after which the outputs of the two tasks were combined.

The four-class classification models directly output the four motion labels F-NL, F-C, B-NL, and B-C. The dual-task models decomposed the four motion classes into two binary-classification tasks. The motion-direction task distinguished between forehand and backhand, whereas the stroke-mode task distinguished between lift and clear. The motion class was ultimately determined by combining the predictions from the two tasks.

The conditional dual-task model first used the 32-dimensional spatial-relation features to establish a motion-direction classifier, with 24 direction-related features retained from the candidate features. After a test sample was predicted as forehand or backhand, it was directed to the corresponding stroke-mode classification branch. Both the forehand- and backhand-conditioned branches used the 80-dimensional hybrid features as candidate inputs and separately retained 16 features to distinguish between lift and clear. The four-class motion label was ultimately obtained by combining the motion-direction output with the direction-conditioned stroke-mode output. This model is designated as "Conditional dual" in Fig. 6.

S2.4 Model training and parameter selection

All classification models used one-way analysis of variance for feature selection within each training fold, followed by classification using a radial basis function (RBF) kernel support vector machine (SVM). The RBF kernel was defined as

$$\mathbf{K}(\mathbf{x}_i,\mathbf{x}_j)=\exp\left(-\gamma\|\mathbf{x}_i-\mathbf{x}_j\|^2\right) \quad \text{(S10)}$$

where γ controls the width of the RBF kernel. Each feature was standardized using the mean and standard deviation of the training set, and the test set was transformed using the same standardization parameters determined from the training set. Class weights were adjusted according to the number of samples in each class within the training set to reduce the influence of slight class imbalance.

The candidate values for the support vector machine penalty parameter C were $C \subset \{0.5, 2, 10, 50\}$. The candidate settings for the radial basis function kernel parameter γ were $\gamma \subset \{\gamma_{adaptive}, 0.001, 0.01, 0.03\}$, where $\gamma_{adaptive}$ denotes the variance-adaptive setting calculated from the corresponding training features. The optimal C–γ combination was determined through four-fold stratified cross-validation within the training set.

Feature selection, feature standardization, class-weight calculation, and parameter selection were performed only within the corresponding training fold. The test samples were not involved in any model-selection procedure or in the estimation of data-transformation parameters.

S2.5 Sequential-block validation and performance evaluation

Model performance was evaluated using five-block validation based on acquisition order. For each motion class, the samples were divided into five consecutive blocks according to their original acquisition order. In each validation round, blocks with the same index from all four motion classes were jointly used as the test set, while the remaining blocks were used as the training set. Five validation rounds were performed so that all 136 samples received one out-of-fold prediction.

All single-unit models, direct four-class classification models, dual-task models, and the conditional dual-task model used identical outer data partitions to ensure comparability of their performance. Model performance was evaluated using accuracy, balanced accuracy, and macro-averaged F1 score. The 95% confidence interval for accuracy was calculated using the Wilson method. In the confusion matrices, the true classes were arranged as rows, and both the row-normalized proportions and corresponding sample counts were reported.

The two-dimensional coordinates used in Fig. 6(e) and Fig. S6(a) were obtained by mapping the support vector machine decision scores to the range of 0–1 using a sigmoid function. The value of 0.5 was used only as a visualization boundary in the figures, and the mapped values were not interpreted as calibrated class probabilities.

Figure S6(c) reports the number of times each feature was selected in the motion-direction branch across the five outer validation folds. Figure S6(d) reports the feature-selection frequencies across 10 branch-model fits for the forehand- and backhand-conditioned stroke-mode branches.